Infrared Spectroscopic Probe of Charge Distribution in Gated Multilayer Graphene: Evidence of Nonlinear Screening

Jiho Kim[1,2] Jiwon Jeon,[1] Byoungju Lee,[1] Kwangnam Yu,[1] Marcelo A. Kuroda[3,*] and E. J. Choi[1,†]

[1] *Department of Physics, University of Seoul, Seoul 02504, South Korea*
[2] *12D IRS Beamline, Pohang Accelerator Laboratory, Pohang 37673, South Korea*
[3] *Department of Physics, Auburn University, Auburn, AL 36849, USA*

We characterize the charge distribution in ion-gated turbostratic multilayer graphene employing broadband infrared transmittance spectroscopy. The experimental results evince the nonlinear screening of graphene and are in agreement with a theoretical model that accounts for the electrostatic coupling between the layers and the quantum capacitance of the graphene. We find that descriptions of charge distributions in these systems in the high-density regimes accessed experimentally via the formation of an electric double layer must include the capacitance of the multilayer graphene channel, which varies with charge and thickness. Specifically, the graphene-channel capacitance increases with thickness but tends to saturate after three layers, underscoring graphene's qualities for ultrathin charge-storage applications. Through accurate determination of the layer-resolved carrier density in multilayer graphene, this sensitive technique may prove useful for the study of charge distributions in other two-dimensional multilayer devices.

I. INTRODUCTION

Since its isolation, graphene has spawned the vast area nowadays known as two-dimensional materials [1, 2]. Its reduced dimensionality and peculiar electronic structure turn this atom-thick layered material into a unique platform for novel physical phenomena, such as the quantum Hall effect [3,4] and unconventional superconductivity [5]. Moreover, a conjunction of remarkable physical properties [6]—including its Young's modulus, thermal conductivity, carrier mobility, and optical transmittance—and progress in the synthesis of large-scale films [7] have also drawn attention to potential technological applications. These include flexible transparent conducting electrodes [8,9], water desalination [10], and broadband electro-optic modulators [11,12], among others. For several of these applications, understanding the charge distribution in multilayer graphene (MLG) is important. For instance, it impacts the effective sheet conductance in optoelectronic devices. In addition, large charge and energy densities in thin electrodes are desired to improve the efficiency of supercapacitor applications [13].

Experimentally, the charge distribution in these layered materials has been studied using a variety of approaches, such as angle-resolved photoemission spectroscopy [14], Kelvin probe force microscopy [15], electrostatic force microscopy [16], midinfrared pump-probe spectroscopy [17], and capacitance measurements using electric double layers (EDLs) [18,19]. These experiments demonstrated that in graphene multilayers, the interfacial capacitance has a quantum origin [20]. Simultaneously, different models have been proposed to describe the charge distribution in multilayers, ranging from analytical methods [16,21–23] to first-principles calculations [24,25]. These models revealed that the charge distribution is highly nonlinear and, owing to the peculiar dispersion of graphene, depends on the relative orientation between the graphene layers [26,27]. To this end, the capability to directly probe the charge density in individual layers is key to testing these models and give insights that could advance charge storage in these systems.

In the work presented here, we perform broadband infrared transmission measurements to characterize the charge distribution in multilayer graphene devices with thicknesses of up to five layers. The turbostratic MLG stacks are gated using an ionic-liquid (IL) electrolyte and probed via Fourier-transform infrared (FTIR) spectroscopy. The charge distributions induced via these EDLs demonstrate the nonlinear screening proposed previously

*mkuroda@auburn.edu
†echoi@uos.ac.kr

for turbostratic graphene. We quantify the contributions to the gate capacitance stemming from the dielectric capacitance and the MLG capacitance. Moreover, our results show that the gate-dependent quantum capacitance of graphene dominates for low carrier densities in these IL-gated devices. This feature becomes more pronounced below three layers. This work shows that the combination of optical spectroscopy and IL gating yields sufficient accuracy to resolve charge distributions in these layered systems. Furthermore, it may allow charge distributions in other devices based on two-dimensional materials and heterostructures of such materials to be probed in a noninvasive and nondestructive manner.

II. EXPERIMENTAL METHODS

We synthesize monolayer graphene sheets using a chemical vapor deposition method and transfer individual layers onto an Al_2O_3 [0001] substrate [7,28–30]. The transfer procedure is successively repeated N times to form multilayer samples ($N \leq 5$). Then we characterize the optical transmission of the resulting MLG with photon energies ranging from the infrared to the ultraviolet (0.25–6 eV). Figure 1(a) shows that the transmission

levels decrease proportionally to the sample thickness N, while the spectral profile remains unchanged. These features are in sharp contrast with the strongly thickness-dependent spectral profile of multilayer graphene with a Bernal or rhombohedral stacking order [31,32], and confirm the turbostratic nature of our samples. On the MLG, we evaporate titanium (5 nm) and gold (100 nm) to form source and drain electrodes. In addition, a separate electrode that serves as a gate is deposited directly on top of the substrate, as shown in Fig. 1(b). We apply an IL electrolyte, 1-ethyl-3-methylimidazolium bis(trifluoromethylsulfonyl)imide (EMIM[TFSI], Merck), covering both the MLG and the gate, to create the EDL-gated device. The broadband infrared transmittance of the MLG devices is measured using a Fourier-transform spectrometer (Bruker Vertex 70 V and Hyperion 2000) over a range of 0.25–1.3 eV. (For $E < 0.25$ eV, data are unavailable because the Al_2O_3 substrate becomes opaque.) Complementarily, we obtain the I–V characteristics of these devices to determine the charge-neutrality point (CNP). All measurements are carried out under ambient conditions. Further details of the ionic-liquid gating and optical measurements can be found in previous publications [33,34].
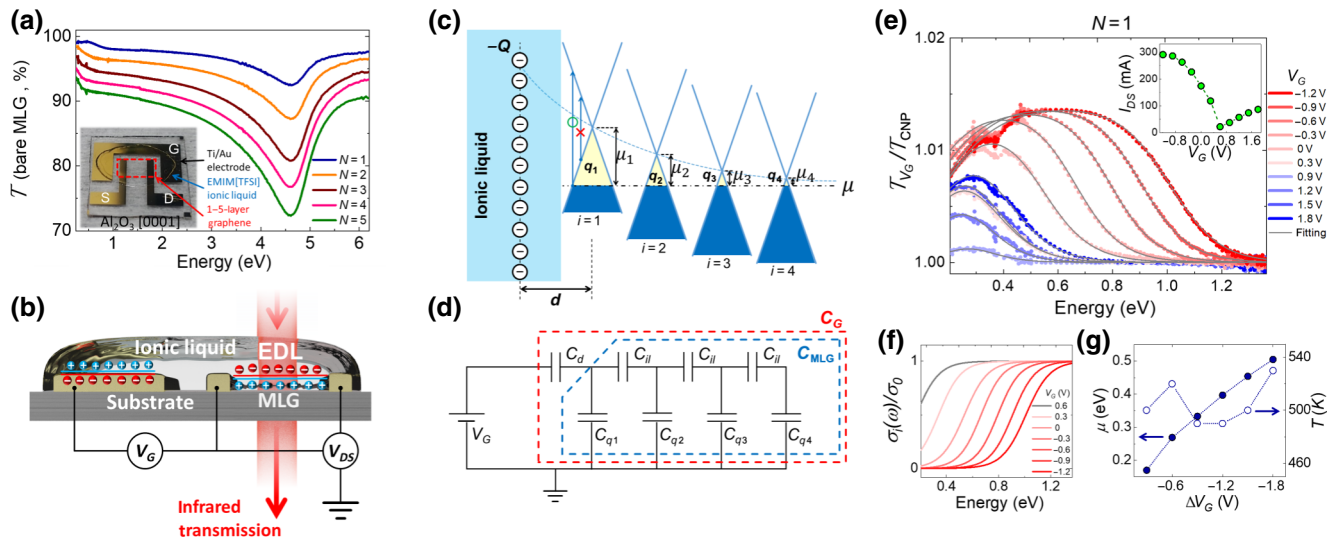

FIG. 1.   (a) Optical transmittance of MLG samples ($N = 1$ to 5) measured without ionic liquid over a wide energy range, 0.25–6.2 eV. The inset shows an image of an actual device with ionic liquid. The red dotted line indicates the region of the graphene channel (3×3 mm^2). (b) Illustration of IL-gated MLG device with infrared transmission measurement. (c) Schematic band diagram of gated MLG stack for $N = 4$. The induced charge Q is distributed across the layers, shifting the position of the chemical potential of each layer relative to its charge-neutrality (Dirac) point. Optical transitions promote electrons in the valence band to the conduction band when the photon energy $E \geq 2|\mu_i|$ (green circle) and are suppressed if $E < 2|\mu_i|$ (red cross). The thickness of the EDL is labeled d. (d) The equivalent capacitor network of the MLG devices includes the capacitance of the dielectric (ionic liquid, C_d), the charge-dependent quantum capacitance of each graphene monolayer ($C_{q,i}$), and the capacitance due to the interlayer spacing (C_{il}). The total capacitance C_G and the series arrangement of the capacitance C_{MLG} are indicated by red and blue dashed lines, respectively. (e) Transmission ratio $\mathcal{T}_{V_G}/\mathcal{T}_{CNP}$ as a function of photon energy E for different gate voltages V_G measured for a monolayer ($N = 1$) device. The experimental data and corresponding fit are shown by symbols and lines, respectively. The inset shows the I–V_G characteristics of the IL-gated device for $V_{DS} = 10$ mV. (f) Normalized optical conductivity as a function of gate bias as derived from the experimental fit. (g) Chemical potential μ (solid line) and temperature T (open circles) obtained from the fit.

III. RESULTS AND DISCUSSION

A. Infrared transmission data

Figure 1(c) depicts a diagram of the charge distribution in an IL-gated MLG sample ($N = 4$). When a gate voltage V_G is applied, the cations ([EMIM]$^+$) and anions ([TFSI]$^-$) become polarized, leading to the creation of an EDL at the IL-MLG interface. The charge induced in the MLG channel is distributed nonuniformly across the different layers. Consequently, the CNP of each layer moves away from the chemical potential of the system (μ), and the layers near the interface experience the largest displacements. Here we define μ_i as the chemical potential in the ith layer measured relative to its own CNP, where the index i runs from 1 to N.

Under infrared irradiation, electrons in the MLG can undergo a vertical transition from the valence band to the conduction band upon the absorption of a photon [Fig. 1(c)]. For the ith graphene layer, this absorption occurs when the photon energy $E = \hbar\omega \geq 2|\mu_i|$, but such an optical process is absent for $E < 2|\mu_i|$. Therefore, the chemical potential μ_i can be determined by measuring the onset of absorption in the broadband transmission spectrum. It is important to note that this sharp onset is smoothed at a finite temperature T. The optical absorption can be described in terms of the optical conductivity $\sigma_i(\omega)$ [35] as

$$\sigma_i(\omega) = \frac{\sigma_0}{2}\left[\tanh\left(\frac{\hbar\omega + 2\mu_i}{4k_BT_i}\right) + \tanh\left(\frac{\hbar\omega - 2\mu_i}{4k_BT_i}\right)\right], \tag{1}$$

where $\sigma_0 = \pi e^2/(2h) = 6.08 \times 10^{-5}\,\Omega^{-1}$, k_B, and T_i are the conductivity quantum of graphene, the Boltzmann constant, and the temperature, respectively.

We first exemplify the extraction of the chemical potential μ_i from the optical measurements in the case of monolayer graphene ($N = 1$). In Fig. 1(e), we present the optical transmission $\mathcal{T}_{V_G}$ measured for different gate voltages ($-1.2 \leq V_G \leq 1.8$ V) and normalized by $\mathcal{T}_{CNP}$, where $V_{CNP} = 0.6$ V, as shown in the inset. The $\mathcal{T}_{V_G}/\mathcal{T}_{CNP}$ ratio is advantageous over the raw $\mathcal{T}_{V_G}$ data for analysis because the effects of the IL and the substrate are largely canceled by the normalization. In $\mathcal{T}_{V_G}/\mathcal{T}_{CNP}$, the absorption onset $2|\mu_i|$ in $\mathcal{T}_{V_G}$ manifests itself as a reduction in the transmission ratio at the corresponding photon frequency and shifts to higher energy as $|V_G - V_{CNP}|$ increases. For a rigorous quantitative analysis, we solve the multilayer Fresnel equation by performing a curve fit of $\mathcal{T}_{V_G}/\mathcal{T}_{CNP}$ using the Kramers-Kronig-constrained RefFit program [36] (see Refs. [33,34,37,38] for further details). The fitted curves successfully reproduce the experimental results. The values of $\sigma_i(\omega)$ and the fitting parameters (μ_i and T_i) are presented in Figs. 1(f) and 1(g), respectively. This methodology to establish the chemical potential μ_i for the $N = 1$ device can be reliably extended to thicker multilayers, as

we show later. Before we continue, it is worthwhile noting that the transmission $\mathcal{T}_{V_G}$ of monolayer graphene is related to its optical conductivity $\sigma_i(\omega)$ by [39]

$$\mathcal{T}_{V_G}(\omega) \approx \frac{1}{|1 + Z_0\sigma_i(\omega)/(1+n)|^2}, \tag{2}$$

where Z_0 ($= 377\,\Omega$) and n ($= 2.3$) are the impedance of free space and the average refractive index of the substrate and the IL, respectively. In Eq. (2), the term $Z_0\sigma_{V_G}(\omega)/(1+n) \ll 1$, and hence the transmission ratio can be approximated as $\mathcal{T}_{V_G}/\mathcal{T}_{CNP} \approx 1 + [2Z_0/(1+n)][\sigma_i(\omega : CNP) - \sigma_i(\omega : V_G)]$. This expression allows an intuitive understanding of the spectral change in the $\sigma_i(\omega : CNP)$ data in Fig. 1(e): the $\sigma_i(\omega : V_G)$ term gives rise to a high-energy reduction in $\mathcal{T}_{V_G}/\mathcal{T}_{CNP}$, which blueshifts with gating, whereas the $\sigma_i(\omega : CNP)$ term produces a low-energy reduction at $E \sim 0.5$ eV independent of gating. (See Fig. S1 in the Supplemental Material [40] for further details.)

In the $\mathcal{T}_{V_G}/\mathcal{T}_{CNP}$ data for two-layer ($N = 2$) graphene (Fig. 2), two absorption onsets appear instead of one, which become more evident as V_G moves away from V_{CNP}. The two onsets are attributed to the fact that each layer has
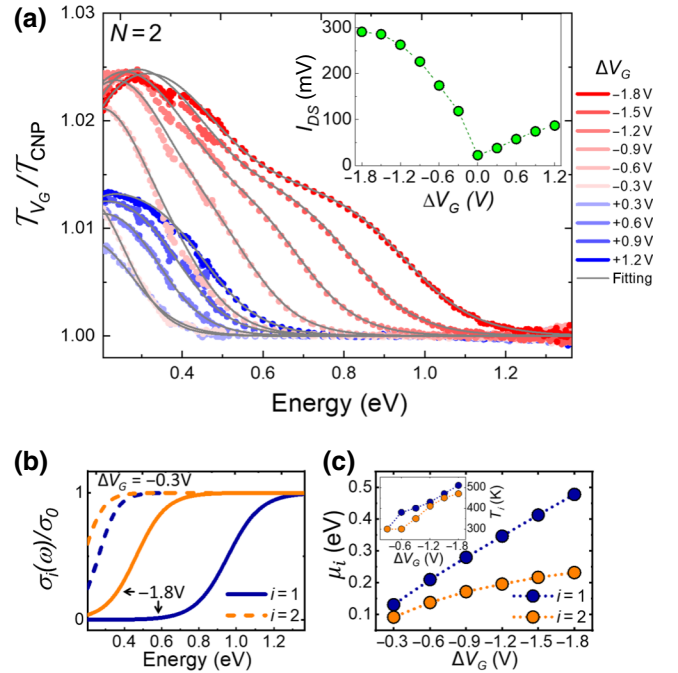

FIG. 2. (a) Experimental data for $\mathcal{T}_V/\mathcal{T}_{CNP}$ (symbols) and theoretical fitting curves (gray lines) in IL-gated bilayer graphene ($N = 2$) for different gate biases ($\Delta V_G = V_G - V_{CNP}$). The inset shows the $I-V_G$ characteristics of the IL-gated device for $V_{DS} = 10$ mV. (b) Optical conductivity obtained from the fit for weak gating $\Delta V_G = -0.3$ V (dashed line) and strong gating $\Delta V_G = -1.8$ V (solid line). Here $i = 1$ (2) stands for the top (bottom) graphene layer as defined in Fig. 1(c). (c) Chemical potential μ_i and temperature T_i (inset) obtained from the fit.

a different chemical potential, $|\mu_1| > |\mu_2|$, due to the electrostatic screening as illustrated in Fig. 1(c). We perform a fit of $\mathcal{T}_{V_G}/\mathcal{T}_{\text{CNP}}$ with $\sigma_1(\omega)$ and $\sigma_2(\omega)$ assigned to the first ($i = 1$) and the second ($i = 2$) layer, respectively. The fitting results for $\sigma_i(\omega)$ are displayed for $\Delta V_G = -0.3$ eV and $\Delta V_G = -1.8$ eV in Fig. 2(b). (From hereon we use ΔV_G to refer to the gate bias relative to the CNP bias, i.e., $\Delta V_G \equiv V_G - V_{\text{CNP}}$.) For the low gate bias $\Delta V_G = -0.3$ eV, $\mu_1 = 0.13$ eV and $\mu_2 = 0.17$ eV are obtained. At the high bias $\Delta V_G = -1.8$ eV, μ_2 separates further from μ_1, making the two onsets clearly distinguishable in $\mathcal{T}_{V_G}/\mathcal{T}_{\text{CNP}}$. The gate-dependent μ_1 and μ_2 are shown in Fig. 2(c). We remark that to assess the accuracy of the fitting we perform a series of calculations, which demonstrate a high confidence level for the parameters obtained (see Fig. S2 in the Supplemental Material). For thicker IL-gated MLGs ($N = 3$, 4, and 5), we carry out similar measurements and analyses, and successfully obtain layer-resolved μ_i and T_i for all layers $1 \le i \le N$. The data and fit are shown in Fig. S3 in the Supplemental Material.

B. Charge distributions

Based on the experimental determination of μ_i and T_i, we obtain the layer-resolved charge distribution as a function of gate bias for different values of N. This is done by calculating the charge density accumulated in each layer as

$$n_i = \frac{2}{\pi(\hbar v_F)^2} \left\{ \int_{-\infty}^{0} [f(E) - 1] |E| \, dE + \int_{0}^{\infty} f(E) |E| \, dE \right\}, \tag{3}$$

where $f(E) = [\exp[(E - \mu_i)/k_B T_i] + 1]^{-1}$ and $D(E) = 2|E|/[\pi(\hbar v_F)^2]$ are the Fermi-Dirac distribution and the electronic density of states of graphene, respectively. We employ the $D(E)$ of monolayer graphene here because turbostratic MLG can be approximated as a stack of independent layers [27]. $\hbar$ and $v_F \approx 1.0 \times 10^8$ cm/s denote

the reduced Planck constant and the Fermi velocity of graphene, respectively [41].

In Fig. 3(a), we present the charge distributions n_i obtained for IL-gated devices. Hereafter we focus on the hole-doping regime ($\Delta V_G < 0$), where a wider range of data is available compared with the electron-doping regime ($\Delta V_G > 0$). Several notable behaviors of the charge distributions n_i are observed. First, the decays that the n_i experience become steeper as ΔV_G (the total charge in the MLG channel) increases. Namely, the charges distributed more or less uniformly across the layers at low bias change so as to be predominantly concentrated in the first few layers ($i = 1, 2$). This behavior can be seen clearly in the plot of n_i/n_{tot} displayed in Fig. 3(b), where $n_{\text{tot}} = \sum_i n_i$ is the total charge in the MLG channel. Such a trend leads to a nonexponential decay of n_i at high ΔV_G, which becomes most visible for the $N = 4$ and $N = 5$ devices. These characteristics show clear experimental evidence for nonlinear screening in MLG, which so far has only been discussed theoretically [22].

C. Capacitance analysis

Quantification of the charge accumulated in the MLG channel allows us to investigate the dependence of the capacitance on the bias and the channel thickness. Computation of the total charge density in the multilayer stacks ($n_{\text{tot}} = \sum_i n_i$) as a function of the gate bias ΔV_G suggests a subtle increase in the total capacitance ($C_G \equiv Q/\Delta V_G$, $Q = e n_{\text{tot}}$) with thickness N [Fig. 4(a)]. As previously depicted in Fig. 1(d), the total capacitance C_G emerges from a series arrangement of the dielectric capacitance $C_d \equiv \varepsilon \varepsilon_0/d$ and the capacitance of the graphene multilayer stack C_{MLG}. Here C_d refers to $C_d = Q/V_d$ and is analyzed in Fig. 4(b) by plotting the total charge Q as a function of the voltage drop in the dielectric layer $V_d = \Delta V_G - V_{\text{MLG}}$, where $V_{\text{MLG}} = \mu_1/e$. We extract $C_d = (2.6 \pm 0.2) \, \mu\text{F/cm}^2$ from a linear fit of Q as a function of V_d averaged over
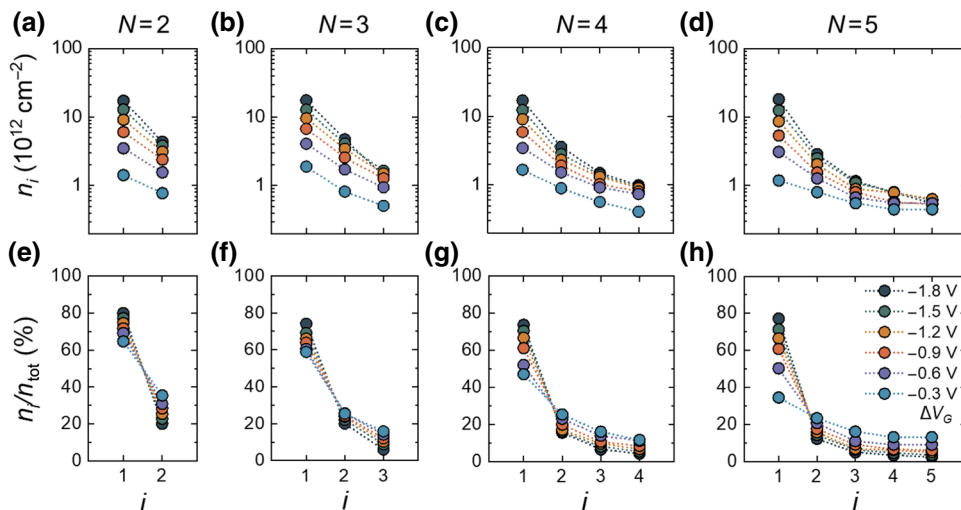

FIG. 3. (a)–(d) Carrier density in the ith layer in IL-gated MLG at different gate biases ΔV_G, where the thickness of the MLG runs from $N = 2$ (left) to $N = 5$ (right). (e)–(h) Corresponding normalized carrier density n_i/n_{tot}.
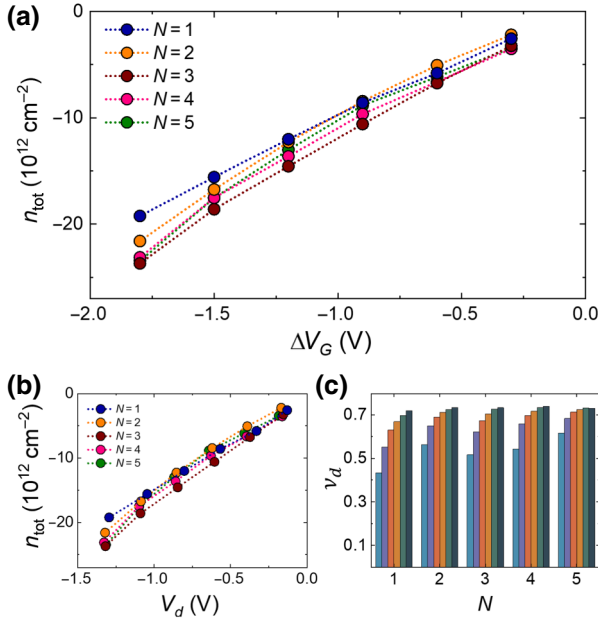
FIG. 4. (a) Total carrier density in the MLG channel as a function of gate bias for different MLG thicknesses ($N = 1$ to 5). (b) Total carrier density as a function of voltage drop across the dielectric layer V_d, as obtained from the experiments. (c) Ratio of the dielectric voltage drop V_d to the gate bias, v_d ($v_d \equiv V_d/\Delta V_G$), for $N = 1$ to 5.
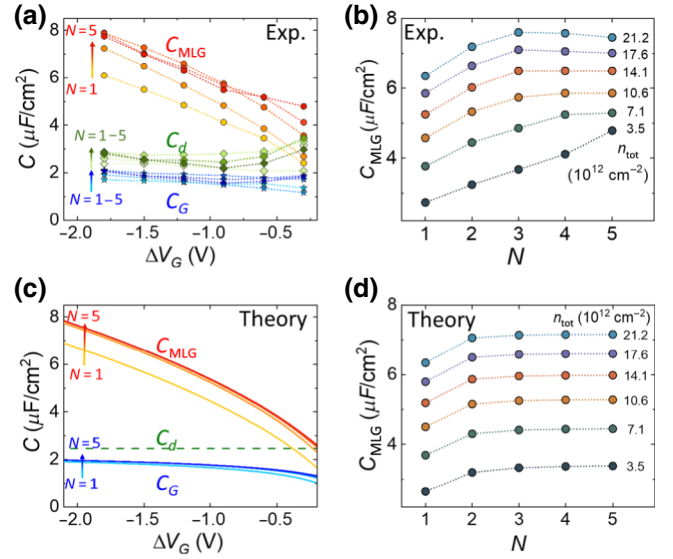

FIG. 5. Capacitances of the system extracted from experiments: (a) total capacitance C_G (stars), dielectric capacitance C_d (diamonds), and MLG capacitance C_{MLG} (circles) as a function of ΔV_G. Different colors denote different layer thicknesses N. (b) MLG capacitance C_{MLG} as a function of N for different charge densities n_{tot}, extracted from interpolation of the experimental data. (c) Theoretical estimates of the gate-dependent capacitances C_d and C_{MLG}, where $C_d = 2.6$ μF/cm^2 is taken from experiment. (d) MLG capacitance C_{MLG} theoretically determined from minimization of the total energy as a function of channel thickness.

the different thicknesses. Unlike the case reported using a different IL [18], the dielectric capacitance C_d of the ionic liquid EMIM[TFSI] shows a weak dependence on the thickness N. Using a dielectric constant of $\varepsilon = 24$ for EMIM[TFSI] [42], these results yield a thickness d of the EDL dielectric [Fig. 1(c)] of approximately 8.5 nm.

Figure 4(c) shows the fraction of the voltage drop in the dielectric layer relative to the total gate bias, $v_d = V_d/\Delta V_G$. As this ratio varies with N and the gate bias, the MLG capacitance $C_{\text{MLG}} \equiv Q/V_{\text{MLG}}$ cannot be treated as constant. Indeed, its relevance becomes more evident for thin channels ($N \leq 3$) and at low gate bias, where $v_d \lesssim 0.5$ for the operating regimes considered in this paper. Thus, the results clearly indicate that at low gate bias (i.e., low charge density) C_{MLG} can become the bottleneck for charge storage in MLG. Below, we discuss further how the bias affects the MLG-channel capacitance and, ultimately, the effective capacitance of the IL-gated device.

In Fig. 5(a), we compare the total capacitance C_G, the dielectric capacitance C_d, and the MLG capacitance C_{MLG} as a function of gate bias for the different Ns. For a fixed bias, C_{MLG} rises moderately with the channel thickness. This increase becomes less noticeable after three layers, i.e., $N \geq 3$. As the gate bias decreases, i.e., a lower charge is induced in the MLG, C_{MLG} reduces by up to a factor of 3 depending on the channel thickness. In Fig. 5(b), we present the capacitance C_{MLG} as a function of the MLG thickness for a fixed carrier density n_{tot}. These curves,

which are compared later with theoretical predictions, are obtained by interpolating experimental results for n_{tot} versus ΔV_G, as we explain in Fig. S4 in the Supplemental Material.

The carrier density profile and corresponding capacitances are calculated theoretically from minimization of the total energy in turbostratic graphene layers [22]. The total energy includes contributions from the filling of bands in the graphene monolayers and the electrostatic interaction between the layers given the total charge Q. From this procedure, the layer-dependent chemical potential μ_i at room temperature is determined, and then the corresponding n_i [Eq. (3)] and capacitance C_{MLG} are computed. Lastly, the gate capacitance C_G is established, given the experimental dielectric capacitance C_d ($= 2.6$ μF/cm^2, Fig. 5).

Figures 5(c) and 5(d) show that the dependences of the capacitances on the gate bias and the MLG thickness, respectively, are in good agreement with the experimental dependences. It should be noted that these calculations assume ideal graphene, ignoring any impurity or defect charge traps in the dielectric layer. In order to unravel the origin of the thickness and bias dependence of the capacitance C_{MLG}, we analyze further the values of its constituents in the experimental regimes accessed in the

present work. The capacitance C_{MLG} is conceived as a combination of the interlayer dielectric capacitances ($C_{\mathrm{il}} \equiv \varepsilon_0/d_{\mathrm{il}} \approx 2.6\,\mu\mathrm{F/cm}^2$) [22,43] and the quantum capacitance of the individual graphene layers $C_{q,i}$ [44]. The latter is given by $C_{q,i} \equiv e^2\,\partial n_i/\partial \mu_i$ [44], which reads

$$C_{q,i} = \frac{4\,k_B T_i\,e^2}{\pi\,(\hbar v_F)^2} \log\left[2\cosh\left(\frac{\mu_i}{2k_B T_i}\right)\right], \qquad (4)$$

after using Eq. (3). It must be noted that Eq. (4) becomes $C_{q,i} = e^2 D(E)$ as $T \to 0$. Estimates derived using Eq. (4) give a value of the quantum capacitance $C_{q,i} = 0.85\,\mu\mathrm{F/cm}^2$ for pristine monolayer graphene ($i = 1$) at room temperature with a low charge density ($|\mu_i| \ll k_B T$), which is about a third of the value of C_d found in these devices. Also, a monolayer holding an excess carrier density of approximately $n_{\mathrm{tot}} = 10^{12}\,\mathrm{cm}^{-2}$ has a quantum capacitance C_q similar to the value of the dielectric capacitance C_d employed here. Hence, the capacitances C_{il} and $C_{q,i}$ forming the MLG capacitance C_{MLG} in the schematic shown in Fig. 1(d) are comparable to C_d, yielding an intricate dependence on the total charge Q, temperature T_i, and number of layers N in IL-gated devices.

D. Related remarks

It is worth mentioning a few minor aspects of the data and their analysis. The I–V_G curves for IL-gated MLG are asymmetric for hole and electron doping, as shown, for example, in the inset of Fig. 2. Empirically, we find that a symmetric I–V_G behavior appears when we add ethyl acetate as a solvent while preparing the IL [33], whereas the asymmetric shape shows up for an IL prepared without it. While the origins of these differences remain elusive, the latter case allows us to achieve a higher carrier density by the use of gating, which is the reason for its adoption in the current experiment.

In the capacitances derived from experiment, deviations are observed at low gate bias (and carrier density), which may be attributed to the inevitable effects of disorder and the substrate smearing the density of states $D(E)$ in the vicinity of the CNP, and spatial charge inhomogeneities [45,46] that effectively yield capacitance values larger than those given by Eq. (4). We also point out that while our discussion of the two sets of fitting parameters (μ_i and T_i) is mainly focused on the chemical potentials μ_i, the broadening that is parameterized as T_i in Eq. (1) differs from the ambient temperature at which the experiment is conducted. This departure may stem from electron-hole puddles produced by impurities and disorder [45], or substrate effects [46,47]. In addition, we remark that the broadening tends to be enlarged as ΔV_G is increased (see Fig. S3), which may be attributed to Joule heating due to the source-drain current I_{DS} that occurs during the I–V_G and IR measurements. Despite these observations, we emphasize that the broadening term T_i does not significantly affect the layer densities n_i computed by use of Eq. (3).

Finally, we examine some differences between our results and previous work on MLG. In some experiments, such as pump-probe measurements [17], a linear screening—yielding charge distributions distinct from those observed here—was reported for exfoliated MLG, which may be attributed to Bernal stacking [21,23], which modifies the Dirac dispersion of turbostratic MLG. Others have reported a thickness dependence of the capacitance [18,19] without providing experimental insights into the layer-resolved carrier distribution or its gate dependence [16]. In the present work, we quantify the carrier density of each layer separately and explicitly characterize the gate dependence of the density profile.

IV. CONCLUSIONS

In conclusion, we perform infrared transmission measurements on ionic-liquid-gated turbostratic multilayer graphene devices with up to five layers. This broadband spectroscopy allows the determination of the chemical potentials of the individual graphene layers, and thus the carrier density profiles in the IL-gated EDL devices and their dependence on the bias. The results clearly show that the charge distributions differ from an exponential decay, providing experimental evidence of nonlinear Coulomb screening in the MLG devices. Furthermore, our theoretical calculations show good agreement with the charge distributions obtained from the experimental results. In terms of charge capacitances, our work reveals that, when ionic-liquid electrolytes are employed, the dielectric capacitance of the EDL (C_d) and the capacitance of the MLG channel (C_{MLG}) are comparable in magnitude. In the high-density regime, C_d is smaller in magnitude than C_{MLG}, which depends on the charge density; in the low-gate-bias regime, the MLG capacitance is nearly constant and becomes the limiting factor for charge accumulation. Our approach provides solid evidence that optimal charge accumulation is reached within a few layers ($N \le 3$) [18,25], which may be exploited in energy-storage applications. The experimental methodology demonstrated in this work may have important implications for the noninvasive characterization of charge distributions in other two-dimensional multilayer devices as well.

[1] A. K. Geim, Nobel lecture: Random walk to graphene, Rev. Mod. Phys. **83**, 851 (2011).

[2] R. Mas-Balleste, C. Gomez-Navarro, J. Gomez-Herrero, and F. Zamora, 2d materials: To graphene and beyond, Nanoscale **3**, 20 (2011).

[3] Y. Zhang, Y.-W. Tan, H. L. Stormer, and P. Kim, Experimental observation of the quantum Hall effect and Berry's phase in graphene, Nature **438**, 201 (2005).

[4] X. Du, I. Skachko, F. Duerr, A. Luican, and E. Y. Andrei, Fractional quantum Hall effect and insulating phase of Dirac electrons in graphene, Nature **462**, 192 (2009).

[5] Y. Cao, V. Fatemi, S. Fang, K. Watanabe, T. Taniguchi, E. Kaxiras, and P. Jarillo-Herrero, Unconventional superconductivity in magic-angle graphene superlattices, Nature **556**, 43 (2018).

[6] A. K. Geim and K. S. Novoselov, in *Nanoscience and Technology: A Collection of Reviews from Nature Journals* (World Scientific, Singapore, 2010), p. 11.

[7] K. S. Kim, Y. Zhao, H. Jang, S. Y. Lee, J. M. Kim, K. S. Kim, J.-H. Ahn, P. Kim, J.-Y. Choi, and B. H. Hong, Large-scale pattern growth of graphene films for stretchable transparent electrodes, Nature **457**, 706 (2009).

[8] X. Li, Y. Zhu, W. Cai, M. Borysiak, B. Han, D. Chen, R. D. Piner, L. Colombo, and R. S. Ruoff, Transfer of large-area graphene films for high-performance transparent conductive electrodes, Nano Lett. **9**, 4359 (2009).

[9] A. Kasry, M. A. Kuroda, G. J. Martyna, G. S. Tulevs ki, and A. A. Bol, Chemical doping of large-area stacked graphene films for use as transparent, conducting electrodes, ACS Nano **7**, 3839 (2010).

[10] S. P. Surwade, S. N. Smirnov, I. V. Vlassiouk, R. R. Unocic, G. M. Veith, S. Dai, and S. M. Mahurin, Water desalination using nanoporous single-layer graphene, Nat Nano **10**, 459 (2015).

[11] M. Liu, X. Yin, E. Ulin-Avila, B. Geng, T. Zentgraf, L. Ju, F. Wang, and X. Zhang, A graphene-based broadband optical modulator, Nature **474**, 64 (2011).

[12] C. T. Phare, Y.-H. D. Lee, J. Cardenas, and M. Lipson, Graphene electro-optic modulator with 30 ghz bandwidth, Nat. Photonics **81**, 511 (2015).

[13] M. F. El-Kady, Y. Shao, and R. B. Kaner, Graphene for batteries, supercapacitors and beyond, Nat. Rev. Mater. **1**, 16033EP (2016).

[14] T. Ohta, A. Bostwick, J. L. McChesney, T. Seyller, K. Horn, and E. Rotenberg, Interlayer Interaction and Electronic Screening in Multilayer Graphene Investigated with Angle-resolved Photoemission Spectroscopy, Phys. Rev. Lett. **98**, 206802 (2007).

[15] N. J. Lee, J. W. Yoo, Y. J. Choi, C. J. Kang, D. Y. Jeon, D. C. Kim, S. Seo, and H. J. Chung, The interlayer screening effect of graphene sheets investigated by Kelvin probe force microscopy, Appl. Phys. Lett. **95**, 222107 (2009).

[16] S. S. Datta, D. R. Strachan, E. J. Mele, and A. T. C. Johnson, Surface potentials and layer charge distributions in few-layer graphene films, Nano Lett. **9**, 7 (2009).

[17] D. Sun, C. Divin, C. Berger, W. A. de Heer, P. N. First, and T. B. Norris, Spectroscopic Measurement of Interlayer Screening in Multilayer Epitaxial Graphene, Phys. Rev. Lett. **104**, 136802 (2010).

[18] E. Uesugi, H. Goto, R. Eguchi, A. Fujiwara, and Y. Kubozono, Electric double-layer capacitance between an ionic liquid and few-layer graphene, Sci. Rep. **3**, 1595 (2013).

[19] H. Ji, X. Zhao, Z. Qiao, J. Jung, Y. Zhu, Y. Lu, L. L. Zhang, A. H. MacDonald, and R. S. Ruoff, Capacitance of carbon-based electrical double-layer capacitors, Nat. Commun. **5**, 3317 (2014).

[20] J. Xia, F. Chen, J. Li, and N. Tao, Measurement of the quantum capacitance of graphene, Nat. Nano **4**, 505 (2009).

[21] M. Koshino, Interlayer screening effect in graphene multilayers with *aba* and *abc* stacking, Phys. Rev. B **81**, 125304 (2010).

[22] M. A. Kuroda, J. Tersoff, and G. J. Martyna, Nonlinear Screening in Multilayer Graphene Systems, Phys. Rev. Lett. **106**, 116804 (2011).

[23] H. Rokni and W. Lu, Layer-by-layer insight into electrostatic charge distribution of few-layer graphene, Sci. Rep. **7**, 42821 (2017).

[24] E. J. G. Santos and E. Kaxiras, Electric-field dependence of the effective dielectric constant in graphene, Nano Lett. **13**, 898 (2013).

[25] M. A. Kuroda, J. Tersoff, R. A. Nistor, and G. J. Martyna, Optimal Thickness for Charge Transfer in Multilayer Graphene Electrodes, Phys. Rev. Appl. **1**, 014005 (2014).

[26] S. Latil and L. Henrard, Charge Carriers in Few-layer Graphene Films, Phys. Rev. Lett. **97**, 036803 (2006).

[27] S. Latil, V. Meunier, and L. Henrard, Massless fermions in multilayer graphitic systems with misoriented layers: Ab initio calculations and experimental fingerprints, Phys. Rev. B **76**, 201402(R) (2007).

[28] X. Li, Y. Zhu, W. Cai, M. Borysiak, B. Han, D. Chen, R. D. Piner, L. Colombo, and R. S. Ruoff, Transfer of large-area graphene films for high-performance transparent conductive electrodes, Nano Lett. **9**, 4359 (2009).

[29] S. Bae, H. Kim, Y. Lee, X. Xu, J.-S. Park, Y. Zheng, J. Balakrishnan, T. Lei, H. R. Kim, Y. I. Song, Y.-J. Kim, K. S. Kim, B. Ozyilmaz, J.-H. Ahn, B. H. Hong, and S. Iijima, Roll-to-roll production of 30-inch graphene films for transparent electrodes, Nat. Nanotechnol. **5**, 574 (2010).

[30] Y. Lee, S. Bae, H. Jang, S. Jang, S.-E. Zhu, S. H. Sim, Y. I. Song, B. H. Hong, and J.-H. Ahn, Wafer-scale synthesis and transfer of graphene films, Nano Lett. **10**, 490 (2010).

[31] K. F. Mak, M. Y. Sfeir, J. A. Misewich, and T. F. Heinz, The evolution of electronic structure in few-layer graphene revealed by optical spectroscopy, Proc. Natl. Acad. Sci. **107**, 14999 (2010).

[32] K. F. Mak, J. Shan, and T. F. Heinz, Electronic Structure of Few-layer Graphene: Experimental Demonstration of Strong Dependence on Stacking Sequence, Phys. Rev. Lett. **104**, 176404 (2010).

[33] K. Yu, J. Jeon, J. Kim, C. W. Oh, Y. Yoon, B. J. Kim, J. H. Cho, and E. J. Choi, Infrared study of carrier scattering mechanism in ion-gated graphene, Appl. Phys. Lett. **114**, 083503 (2019).

[34] K. Yu, N. Van Luan, T. Kim, J. Jeon, J. Kim, P. Moon, Y. H. Lee, and E. J. Choi, Gate tunable optical absorption and band structure of twisted bilayer graphene, Phys. Rev. B. **99**, 241405(R) (2019).

[35] K. F. Mak, M. Y. Sfeir, Y. Wu, C. H. Lui, J. A. Misewich, and T. F. Heinz, Measurement of the Optical Conductivity of Graphene, Phys. Rev. Lett. **101**, 196405 (2008).

[36] A. Kuzmenko, Kramers–Kronig constrained variational analysis of optical spectra, Rev. Sci. Instrum. **76**, 083108 (2005).

[37] K. Yu, J. Kim, J. Y. Kim, W. Lee, J. Y. Hwang, E. H. Hwang, and E. J. Choi, Infrared spectroscopic study of carrier scattering in gated CVD graphene, Phys. Rev. B **94**, 235404 (2016).

[38] L. Ju, B. Geng, J. Horng, C. Girit, M. Martin, Z. Hao, H. A. Bechtel, X. Liang, A. Zettl, Y. R. Shen, and F. Wang, Graphene plasmonics for tunable terahertz metamaterials, Nat. Nanotechnol. **6,** 630 (2011).

[39] C. Lee, J. Y. Kim, S. Bae, K. S. Kim, B. H. Hong, and E. J. Choi, Optical response of large scale single layer graphene, Appl. Phys. Lett. **98**, 071905 (2011).

[40] See the Supplemental Material at http://link.aps.org/supple mental/10.1103/PhysRevApplied.13.014066 for information about the FTIR spectrum of the ionic liquid.

[41] A. H. CastroNeto, F. Guinea, N. M. R. Peres, K. S. Novoselov, and A. K. Geim, The electronic properties of graphene, Rev. Mod. Phys. **81**, 109 (2009).

[42] Y. Xia, J. H. Cho, J. Lee, P. P. Ruden, and C. D. Frisbie, Comparison of the mobility–carrier density relation in polymer and single-crystal organic transistors employing vacuum and liquid gate dielectrics, Adv. Mater. **21**, 2174 (2009).

[43] J. Kumar, M. A. Kuroda, M. Z. Bellus, S.-J. Han, and H.-Y. Chiu, Full-range electrical characteristics of ws2 transistors, Appl. Phys. Lett. **106**, 123508 (2015).

[44] S. Luryi, Quantum capacitance devices, Appl. Phys. Lett. **52**, 501 (1988).

[45] J. Martin, N. Akerman, G. Ulbricht, T. Lohmann, J. H. Smet, K. von Klitzing, and A. Yacoby, Observation of electron–hole puddles in graphene using a scanning single-electron transistor, Nat. Phys. **4**, 144 (2007).

[46] Y. Zhang, V. W. Brar, C. Girit, A. Zettl, and M. F. Crommie, Origin of spatial charge inhomogeneity in graphene, Nat. Phys. **5**, 722 (2009).

[47] J. Sforzini, P. Hapala, M. Franke, G. van Straaten, A. Stöhr, S. Link, S. Soubatch, P. Jelínek, T.-L. Lee, U. Starke, M. Švec, F. C. Bocquet, and F. S. Tautz, Structural and Electronic Properties of Nitrogen-doped Graphene, Phys. Rev. Lett. **116**, 126805 (2016).